PAPER • OPEN ACCESS

Spectral properties and breathing dynamics of a few-body Bose–Bose mixture in a 1D harmonic trap

To cite this article: Maxim Pyzh *et al* 2018 *New J. Phys.* **20** 015006

View the article online for updates and enhancements.

New Journal of Physics

The open access journal at the forefront of physics

PAPER

CrossMark

Spectral properties and breathing dynamics of a few-body Bose–Bose mixture in a 1D harmonic trap

Maxim Pyzh[1,4], Sven Krönke[1,2], Christof Weitenberg[3] and Peter Schmelcher[1,2]

[1] Zentrum für Optische Quantentechnologien, Universität Hamburg, Luruper Chaussee 149, D-22761 Hamburg, Germany
[2] The Hamburg Centre for Ultrafast Imaging, Universität Hamburg, Luruper Chaussee 149, D-22761 Hamburg, Germany
[3] Institut für Laserphysik, Universität Hamburg, D-22761 Hamburg, Germany
[4] Author to whom any correspondence should be addressed.

E-mail: mpyzh@physnet.uni-hamburg.de and pschmelc@physnet.uni-hamburg.de

Abstract

We investigate a few-body mixture of two bosonic components, each consisting of two particles confined in a quasi one-dimensional harmonic trap. By means of exact diagonalization with a correlated basis approach we obtain the low-energy spectrum and eigenstates for the whole range of repulsive intra- and inter-component interaction strengths. We analyse the eigenvalues as a function of the inter-component coupling, covering hereby all the limiting regimes, and characterize the behaviour in-between these regimes by exploiting the symmetries of the Hamiltonian. Provided with this knowledge we study the breathing dynamics in the linear-response regime by slightly quenching the trap frequency symmetrically for both components. Depending on the choice of interactions strengths, we identify 1 to 3 monopole modes besides the breathing mode of the centre of mass coordinate. For the uncoupled mixture each monopole mode corresponds to the breathing oscillation of a specific relative coordinate. Increasing the inter-component coupling first leads to multi-mode oscillations in each relative coordinate, which turn into single-mode oscillations of the same frequency in the composite-fermionization regime.

1. Introduction

The physics of ultra-cold atoms has gained a great boost of interest since the first experimental realization of an atomic Bose–Einstein condensate [1, 2], where research topics such as collective modes [3–5], binary mixtures [6, 7] and lower-dimensional geometries [8–10] were in the focus right from the start. In most of the experiments on ultra-cold gases the atoms are but weakly correlated and well described by a mean-field (MF) model, the well-known Gross–Pitaevskii equation (GPE), or in case of mixtures by coupled GPEs [11–13]. Bose–Bose mixtures exhibit richer physics compared to their single component counterpart. For instance, different ground state profiles can be identified depending on the ratios between the intra- and inter-species interaction strengths, being experimentally tunable by e.g. Feshbach resonances (FRs) [14]: the miscible, immiscible symmetry-broken (SB) or immiscible core–shell structure, also called phase separation (PS) [15–17]. Comparing the experimentally obtained densities to numerical MF calculations [18, 19] provides a sensitive probe for precision measurements of the scattering lengths or, if known, the magnetic fields used to tune them [16]. Another possibility to access the interaction regime and thus the scattering lengths is by exciting the system and extracting the frequencies of low-lying excitations [20]. In contrast to a single-species case the collective modes of mixtures exhibit new exciting phenomena: doublet splitting of the spectrum containing in-phase and out-of-phase oscillations, mode-softening for increasing inter-component coupling, onset of instability of the lowest dipole mode leading to the SB phase as well as minima in the breathing mode frequencies w.r.t. interaction strength [21–23].

The breathing or monopole mode, characterized by expansion and contraction of the atomic density, has in particular proven to be a useful tool for the diagnostics of static and dynamical properties of physical systems. It

is sensitive to the system's dimensionality, spin statistics as well as form and strength of interactions [24–27]. In the early theoretical investigations on quasi-one-dimensional single-component systems [28] it was shown that different interaction regimes can be distinguished by the breathing mode frequency, which has been used in experiments [10, 29, 30]. Furthermore, the monopole mode provides indirect information on the ground state [31], its compressibility [32] and the low-lying energy spectrum such that an analogy has been drawn to absorption/emission spectroscopy in molecular physics [27].

From a theoretical side, those of the above experiments which are concerned with quasi-1D set-ups are in particular interesting, since correlations are generically stronger, rendering MF theories often inapplicable. Here, confinement induced resonances (CIR) [8] can be employed to realize the Tonks–Girardeau limit [33, 34], where the bosons resemble a system of non-interacting fermions in many aspects. While this case can be solved analytically [35, 36], strong but finite interactions are tractable only to numerical approaches, which limits the analysis to few-body systems. For instance, a profound investigation of the ground state phases of a few-body Bose–Bose mixture [37, 38] showed striking differences to the MF calculations: for coinciding trap centres, a new phase with bimodal symmetric density structure, called composite fermionization (CF), is observed while SB is absent for any finite inter-component coupling. Only in the limit of infinite coupling the ground state becomes two-fold degenerate enabling to choose between CF and SB representations [39], while the MF theory predicts the existence of SB already for finite couplings. This observation accentuates the necessity to include correlation effects.

In this work we solve the time-independent problem of the simplest Bose–Bose mixture confined in a quasi-1D HO trap with two particles in each component, covering the whole parameter space of repulsive intra- and inter-species interactions, thereby complementing the analysis of some previous studies [39–41]. To accomplish this, an exact diagonalization method based on a correlated basis is introduced. We unravel how the distinguishability of the components renders the spectrum richer and complexer compared to a single component case [42]. Furthermore, these results are used to investigate the breathing dynamics of the composite system. While the breathing spectrum of a single component was recently investigated comprehensively in [43–49], reporting a transition from a two mode beating of the centre of mass Ω_{CM} and relative motion Ω_{rel} frequencies for few atoms to a single mode breathing for many particles, the breathing mode properties of few-body Bose–Bose mixtures are not characterized so far. For this reason, we analyse the number of breathing frequencies and the kind of motion to which they correspond in dependence on the intra- and inter-component interaction for the binary mixture at hand.

This work is structured as follows. In section 2 we introduce the Hamiltonian of the system. In section 3 we perform a coordinate transformation to construct a fast converging correlated basis. Using exact diagonalization with respect to this basis we study in section 4 the low-lying energy spectrum for various interaction regimes. Section 5 is dedicated to the breathing dynamics within the linear response regime. An experimental realization is discussed in section 6 and we conclude the paper with a summary and an outlook in section 7.

2. Model

We consider a Bose–Bose mixture containing two components, which are labelled by $\sigma \in \{A, B\}$, confined in a highly anisotropic harmonic trap. We assume the low temperature regime, where the inter-particle interactions may be modelled via a contact potential, and strong transversal confinement allowing us to integrate out frozen degrees of freedom leading to a quasi-1D model. Our focus lies on a mixture of $N_\sigma = 2$ particles, which have the same mass $m_\sigma \equiv m$ and trapping frequencies $\omega_{\sigma,\perp} \equiv \omega_\perp, \omega_{\sigma,\parallel} \equiv \omega$ in the transversal, longitudinal direction, respectively. This can be realized by choosing different hyperfine states of the same atomic species. By further rescaling the energy and length in units of $\hbar\omega$ and $a_{\text{ho}} = \sqrt{\hbar/(m\omega)}$ one arrives at the dimensionless Hamiltonian:

$$H = \sum_\sigma H_\sigma + H_{AB}, \tag{1}$$

with the single-component Hamiltonians H_σ

$$H_\sigma = \sum_{i=1}^{2}\left(-\frac{1}{2}\frac{\partial^2}{\partial x_{\sigma,i}^2} + \frac{1}{2}x_{\sigma,i}^2\right) + g_\sigma\delta(x_{\sigma,1} - x_{\sigma,2}), \tag{2}$$

and inter-component coupling H_{AB}

$$H_{AB} = g_{AB}\sum_{i,j=1}^{2}\delta(x_{A,i} - x_{B,j}), \tag{3}$$

where $g_\alpha \approx (2a_\alpha^{\text{3D}}\omega_\perp)/(\omega a_{\text{ho}})$ with a_α^{3D} the 3D s-wave scattering length and $\alpha \in \{A, B, AB\}$ are effective (off-resonant) interaction strengths.

3. Methodology: exact diagonalization in a correlated basis

To obtain information on the low-energy excitation spectrum we employ the well-established method of exact diagonalization [50]. However, instead of taking bosonic number states w.r.t. HO eigenstates for the underlying basis as done in e.g. [40], we pursue a different approach by using a correlated atom-pair basis. This allows us to study arbitrary intra-component interactions g_σ (even infinity) exactly, whereas HO number states are much more inefficient in handling strong intra-component interactions. At the same time our method converges quickly for inter-component couplings $g_{AB} \leqslant 10$ requiring at most 700 basis states. In comparison, a straightforward treatment in the laboratory frame requires typically $\sim 10^5$ HO number states for obtaining converged ground-state results [38]. For even larger g_{AB} couplings, the chosen basis becomes less appropriate such that our basis size has then to be significantly increased in order to obtain accurate results. Going, however, beyond $g_{AB} = 10$ would not give qualitatively new physical phenomena. Essentially all effects of the strong-coupling regime can be investigated by studying the crossover from $g_{AB} = 0$ to $g_{AB} = 10$.

Actually, the idea of choosing optimized basis sets to speed up the convergence with respect to the size of basis functions can be also seen in the context of the potential-optimized discrete variable representation [51]. Here, one employs eigenstates of conveniently constructed one-dimensional reference Hamiltonians in order to incorporate more information on the actual Hamiltonian into the basis compared to the standard DVR technique [52, 53]. Another approach, stemming from nuclear physics, uses an effective two-body interaction potential instead of an optimized basis for solving ultra-cold many-body problems [54–56].

In order to construct a tailored basis, which already incorporates intra-component correlations, we apply a coordinate transformation to the relative frame $\vec{Y} \equiv (R_{CM}, R_{AB}, r_A, r_B)^T$ defined by:

- total CM coordinate

$$R_{CM} = \sum_\sigma \sum_{i=1}^2 x_{\sigma,i}/4,$$

- relative CM coordinate

$$R_{AB} = \sum_{i=1}^2 x_{A,i}/2 - \sum_{i=1}^2 x_{B,i}/2,$$

- relative coordinate for each σ component

$$r_\sigma = x_{\sigma,1} - x_{\sigma,2}.$$

In this frame, the Hamiltonian (1) attains the following form:

$$H = H_{R_{CM}} + H_{R_{AB}} + \sum_{\sigma=A,B} H_{r_\sigma} + g_{AB}H_1. \tag{4}$$

Here, the total CM separates, $H = H_{R_{CM}} + H_{\text{rel}}$, and is simply governed by a harmonic oscillator (HO) Hamiltonian with mass $M = 4$:

$$H_{R_{CM}} = -\frac{1}{8}\frac{\partial^2}{\partial R_{CM}^2} + 2R_{CM}^2, \tag{5}$$

featuring the spectrum $E_n^{CM} = n + 1/2$ with $n \in \mathbb{N}_0$. The remainder of the Hamiltonian can be decomposed as $H_{\text{rel}} = H_0 + g_{AB}H_1$, where $H_0 = H_{R_{AB}} + \sum_\sigma H_{r_\sigma}$ can be solved analytically and H_1 couples the eigenstates of H_0:

$$H_{R_{AB}} = -\frac{1}{2}\frac{\partial^2}{\partial R_{AB}^2} + \frac{1}{2}R_{AB}^2, \tag{6}$$

$$H_{r_\sigma} = -\frac{\partial^2}{\partial r_\sigma^2} + \frac{1}{4}r_\sigma^2 + g_\sigma \delta(r_\sigma), \tag{7}$$

$$H_1 = \sum_{i,j=1}^2 \delta\left(R_{AB} + (-1)^i\frac{r_A}{2} + (-1)^j\frac{r_B}{2}\right). \tag{8}$$

So $H_{R_{AB}}$ is a HO Hamiltonian of mass $M = 1$ and H_{r_σ} leads to the Weber differential equations[5] for its eigenstates with delta-function constraint. The corresponding solutions are normalized as well as symmetrized parabolic

---

[5] $f''(r) + (\mu + \frac{1}{2} - \frac{1}{4}r^2)f(r) = 0$ with $r \in \mathbb{R}$ and $\mu \in \mathbb{R}$.

cylinder functions[6] (PCF) $\varphi_n^\sigma(r_\sigma) \propto D_{\mu(g_\sigma,n)}(|r_\sigma|)$ of the relative coordinate with $\mu(g_\sigma,\, n)$ being a real valued quantum number depending on the intra-component interaction strength g_σ and the excitation level $n \in \mathbb{N}_0$, which is obtained by solving a transcendental equation stemming from the delta-function constraint [57]:

$$g_\sigma = -2^{\frac{3}{2}} \frac{\Gamma\left(\frac{1-\mu}{2}\right)}{\Gamma\left(-\frac{\mu}{2}\right)}. \tag{9}$$

Now to diagonalize H_{rel} we choose the eigenvectors of H_0 as basis states and label them as $|k,\, l,\, m\rangle$ with $k,\, l,\, m \in \mathbb{N}_0$. Their spatial representation and corresponding eigenenergies read:

$$\langle R_{AB},\, r_A,\, r_B | k,\, l,\, m \rangle = \Phi_k^{AB}(R_{AB})\, \varphi_l^A(r_A)\, \varphi_m^B(r_B), \tag{10}$$

$$E_{k,l,m}^{(0)} = k + \mu(g_A,\, l) + \mu(g_B,\, m) + \frac{3}{2}, \tag{11}$$

where Φ_k^{AB} are HO eigenstates of $H_{R_{AB}}$. We note that all $\varphi_i^\sigma(r_\sigma)$ are of even parity because of the bosonic nature of the particles of each component.

The main challenge now is the calculation of the matrix elements of H_1, which are complicated 2D integrals at first sight and need to be tackled numerically. In the appendix we provide a circumvention of this problem via the Schmidt decomposition [58], allowing us to replace one 2D integral by multiple 1D integrals, which results in faster computation times. In quantum chemistry, the algorithm for achieving such a representation is known as POTFIT [59]. In the appendix, we moreover point out several symmetries which can be utilized for efficiently evaluating these 1D integrals and discuss in detail, why our computational strategy is much more efficient than the direct evaluation of the 2D integrals for the problem at hand.

To summarize, the coordinate transformation to the chosen relative frame (i) decouples the CM motion and (ii) naturally guides us to employ the analytically known eigenstates of H_0 as the basis states in order to incorporate intra-component correlations into our basis.

4. Stationary properties

By means of the correlated basis introduced above and an efficient strategy for calculating the Hamiltonian matrix to be diagonalized, we can easily obtain the static properties of our system for arbitrary intra-component interaction strengths g_σ and inter-component coupling $g_{AB} \leqslant 10$. The most representative choices of interaction strengths (g_A, g_B, g_{AB}) are the subject of this section and in order to get a deeper understanding of the spectral properties a thorough discussion of the symmetries of H is necessary.
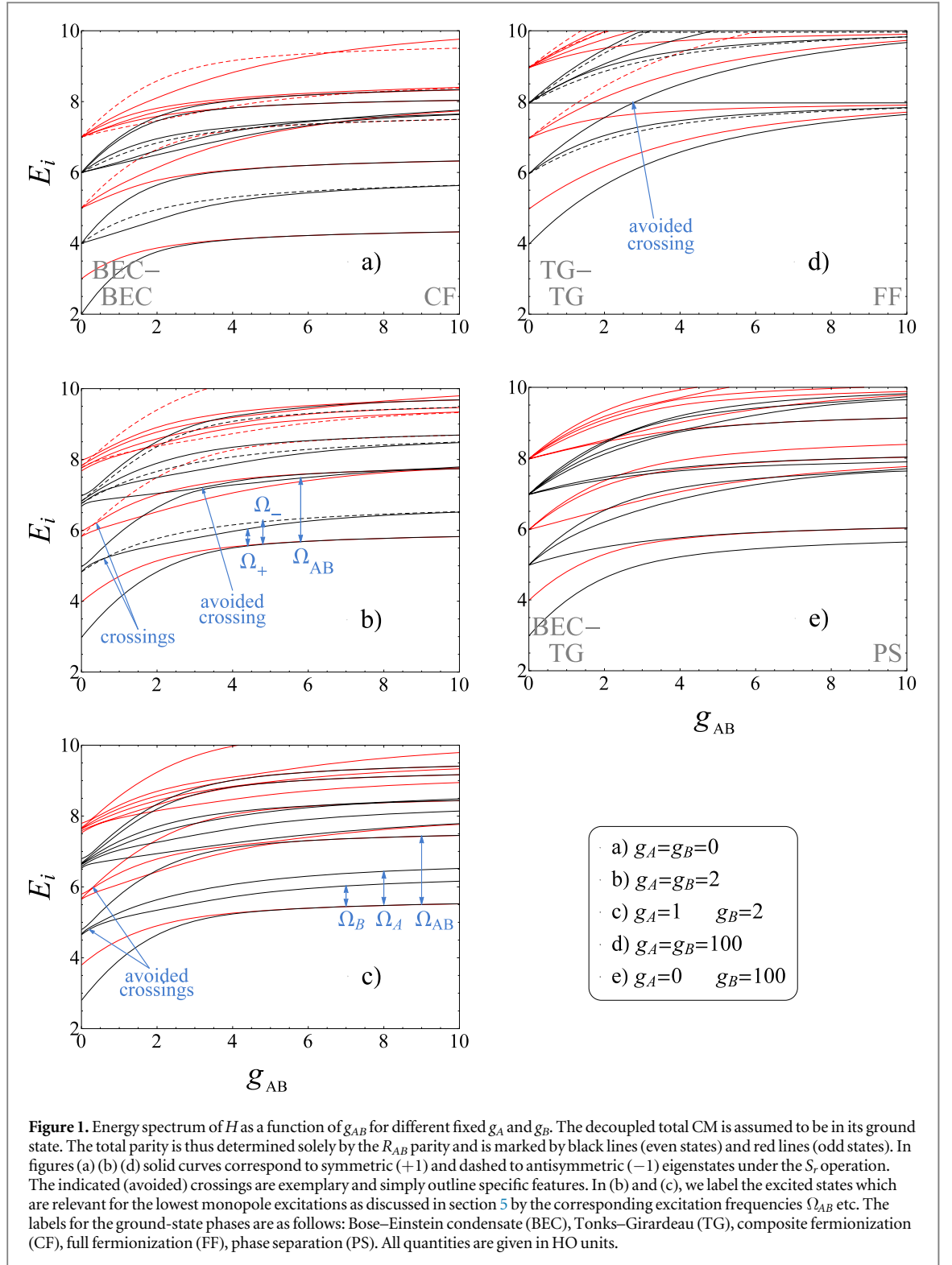
4.1. Symmetry analysis
In the laboratory frame, there are only a few obvious symmetries: (i) the total parity P_{tot} (i.e. simultaneous replacement of all coordinates $x_{\sigma,i}$ by $-x_{\sigma,i}$), (ii) an interchange of the two A particles S_A or of the two B particles S_B, (iii) in the case of equal intra-component couplings $g_A = g_B$ a simultaneous interchange of two A particles with two B particles S_{AB} and (iv) given all couplings to be equal, the exchange S_{ij} of any two particles being labelled by i, j. In the relative frame though, additional symmetries become apparent. The total Hamiltonian H commutes with each individual parity operator P_{Y_i} of the relative frame coordinates (P_{Y_i} replaces Y_i by $-Y_i$ while leaving the other coordinates of the relative frame invariant). In these regards, we note that $P_{R_{AB}}$ does not commute with the individual terms in equation (8) but only with the whole sum of these four terms. The eigenvectors of P_{r_σ} are restricted to even parity because of the bosonic character of our components, corresponding to the S_σ operation. In contrast to the former operations, the symmetry transformations $P_{R_{CM}}$ and $P_{R_{AB}}$ are highly non-trivial in the laboratory frame involving improper rotations of the four-dimensional coordinate system. Due to the decoupling of $H_{R_{CM}}$ it is sufficient to consider only the ground state of the total CM motion, which is of even R_{CM} parity, in the following. Then, the parity of the R_{AB} degree of freedom completely determines the total parity of the eigenstates. Finally, a further symmetry arises if one chooses equal intra-component interaction strengths g_σ. In this case, the Hamiltonian H is invariant under an exchange of the relative coordinates $r_A \leftrightarrow r_B$, which we define as the S_r transformation in the following. Contra-intuitively, S_r is not the same as the S_{AB} transformation. In total, the chosen relative frame indicates a set of additional symmetries, which are hidden in the laboratory frame.

4.2. Energy spectra
In figure 1 we show the total energy spectrum as a function of g_{AB} for various fixed values of g_A and g_B. The total CM is assumed to be in its ground state. Figure 1(a) depicts the non-interacting intra-component scenario

---

[6] $D_\mu(|r|) = 2^{\frac{\mu}{2}} e^{-\frac{r^2}{4}} U\left(-\frac{1}{2}\mu, \frac{1}{2}, \frac{1}{2}r^2\right)$ with $U(a,\, b,\, x)$ denoting the Tricomi's hypergeometric function.

Figure 1. Energy spectrum of H as a function of g_{AB} for different fixed g_A and g_B. The decoupled total CM is assumed to be in its ground state. The total parity is thus determined solely by the R_{AB} parity and is marked by black lines (even states) and red lines (odd states). In figures (a) (b) (d) solid curves correspond to symmetric $(+1)$ and dashed to antisymmetric (-1) eigenstates under the S_r operation. The indicated (avoided) crossings are exemplary and simply outline specific features. In (b) and (c), we label the excited states which are relevant for the lowest monopole excitations as discussed in section 5 by the corresponding excitation frequencies Ω_{AB} etc. The labels for the ground-state phases are as follows: Bose–Einstein condensate (BEC), Tonks–Girardeau (TG), composite fermionization (CF), full fermionization (FF), phase separation (PS). All quantities are given in HO units.

$g_\sigma = 0$. For $g_{AB} = 0$ the Hamiltonian represents two uncoupled non-interacting bosonic species and we will label this regime as BEC–BEC following the nomenclature of [40]. The eigenenergies are integers with equal spacings of $\hbar w$, which is 1 in our units. In this limit the PCFs are even HO eigenstates of mass $m = 1/2$. The eigenenergies are thus $E_{\text{tot}} = E_{n=0}^{\text{CM}} + E_{k,l,m}^{(0)} \equiv E_{0,k,l,m}^{(0)} = k + 2l + 2m + 2$.

For $g_{AB} = 0$, the ith eigenenergy corresponding to only even (odd) R_{AB}-parity eigenstates is $(i + 2)!/(2! i!)$ fold degenerate with $i \in \mathbb{N}_0$. Already a small inter-component coupling lifts all these degeneracies such that branches of eigenenergies arise. In the following, we label these resulting branches as the ith even or odd R_{AB}-parity branch, respectively. Note that this grouping of the energy levels into branches will be used in the following for all values of g_{AB} and in particular for the analysis of the breathing dynamics in section 5. As we further increase the inter-component coupling strength, we observe that states corresponding to branches of

opposite R_{AB}-parity incidentally cross, as they are of different symmetry and consequently not coupled by the H_1 perturbation.

For very strong g_{AB} values, i.e. in the CF limit [37, 38], we observe a restoration of degeneracies, but in a different manner, namely the lowest states merge pairwise forming a two-fold degeneracy. In this regime the two components spatially separate for the ground state, where one component locates on the left side of the trap, while the other is pushed to the right side due to the strong inter-component repulsion. The two-fold degeneracy of the ground state reflects actually the two possible configurations: *A* left *B* right and *A* right *B* left. This behaviour can be observed in the relative frame densities, discussed later in this section. Another striking peculiarity for $g_{AB} \to \infty$ are non-integer eigenvalues and unequal energy spacings, meaning that for CF no 'TG-like' mapping to a non-interacting HO system exists.

A very similar analysis concerning this specific choice of interactions ($g_\sigma = 0$ and arbitrary g_{AB}) was performed in [39], where an effective interaction approach was employed to greatly improve the convergence properties of exact diagonalization in order to access properties of a Bose–Bose mixture with up to $N = 10$ particles. However, the analysis only covered a single line of the (g_A, g_B, g_{AB}) parameter space. Another similar work [40] deals with the system's properties for an even wider range of intra- and inter-component interactions, however the main focus lies on the ground state properties. Here, we extend the analysis of [39, 40] by studying both the ground state and the low-lying excitations for weak, strong as well as intermediate interactions g_α.

In figure 1(b) we show the impact of moderate but symmetric intra-component interactions of strength $g \equiv g_\sigma = 2$. Already in the uncoupled regime ($g_{AB} = 0$) we observe fewer degeneracies compared to the $g_\sigma = 0$ case. Nevertheless, we group the eigenstates into branches of even/odd R_{AB}-parity also for finite g_σ by continuously following the eigenenergies to the $g_\sigma \to 0+$ limit. The reason for the reduced degeneracies is that the PCFs are not HO eigenstates anymore, while the PCFs of both components coincide pairwise. The eigenenergies read $E^{(0)}_{0,k,l,m} = k + \mu(g, l) + \mu(g, m) + 2$. To roughly estimate the energetic ordering it is sufficient to know that the real-valued quantum number $\mu(g, n)$ fulfills for $0 < g < \infty$ the following relations:

- $2n < \mu(g, n) < 2n + 1$

- $\mu(g, n) + 1 < \mu(g, n + 1) < \mu(g, n) + 2$

meaning that a single excitation of the relative motion r_σ is energetically below a double excitation of the R_{AB} degree of freedom. E.g. the first even R_{AB}-parity branch in the uncoupled non-interacting regime (BEC–BEC in figure 1(a)) contains three degenerate states: $|2, 0, 0\rangle$, $|0, 1, 0\rangle$ and $|0, 0, 1\rangle$ (equation (10)). By choosing finite g_σ values $|2, 0, 0\rangle$ acquires a higher energy than $|0, 1, 0\rangle$ and $|0, 0, 1\rangle$ leading to reduced degeneracies in the spectrum. Another striking feature is the appearance of additional crossings between states of the same R_{AB}-parity due to the S_r symmetry. States, which possess different quantum numbers concerning the S_r transformation ($+1$ or -1), are allowed to cross as they 'randomly' do throughout the g_{AB} variation. Of course, such crossings are also present in the previous non-interacting case, it being also component-symmetric. An avoided crossing between a state of the first even R_{AB}-parity branch and a state of the second even R_{AB}-parity branch is worth mentioning, which is present for all values of g_σ (see the exemplary arrow in figures 1(b) or (d)). States of the same symmetry obviously do not cross according to the Wigner-von Neumann non-crossing rule [60].

In figure 1(c) we asymmetrically increase the intra-component interactions g_σ as compared to the non-interacting case, namely to $g_A = 1$ and $g_B = 2$. For the uncoupled scenario ($g_{AB} = 0$) all the degeneracies are lifted, because now PCFs of the *A* and the *B* components are different. The energy is $E^{(0)}_{0,k,l,m} = k + \mu(g_A, l) + \mu(g_B, m) + 2$. The energetic state ordering is far from obvious, which becomes apparent upon closer inspection of the $\mu(g, n)$ function. E.g. consider again the first even R_{AB}-parity branch. Its lowest energy state is a single excitation of r_B, followed by a single excitation of r_A. The highest energy of this branch corresponds to a double R_{AB} excitation. The ordering pattern for higher order branches is even more complicated. For intermediate values of g_{AB} we observe that crossings from the previous scenario (with $g_\sigma = 2$) between states of the same R_{AB}-parity are replaced by avoided crossings because of the broken S_r symmetry. The strong coupling regime displays less degeneracies as compared to the component-symmetric cases of figures 1(a) and (b) with the two-fold ground state degeneracy remaining untouched.

In figure 1(d) we choose very strong intra-component interaction strengths $g_\sigma = 100$. When the g_{AB}-coupling is absent, we have two hard-core bosons in each component. The system can thus be mapped to a two-component mixture of non-interacting fermions [35, 61] and will be referred to as TG–TG limit. The PCFs become near degenerate with odd HO eigenstates, which again leads to integer-valued eigenenergies $E^{(0)}_{0,k,l,m} \approx k + 2l + 2m + 4$ with equal spacings and the same degree of (near-)degeneracies as in the non-interacting case (figure 1(a)). The limit of strong inter-component coupling displays a completely different structure of the spectrum. The so-called full fermionization (FF) [36] phase can be mapped to a non-interacting ensemble of four fermions with the ground state energy $N^2/2 = 8$. However, in contrast to the single-

component case of four bosons, we need to take into account that the components are distinguishable. Thus, the degeneracy of the ground state is expected to be $N!/(N_A!N_B!) = 6$-fold and corresponds to the different possibilities of ordering the laboratory frame coordinates while keeping in mind the indistinguishability of particles of each component. This limit of all interactions strengths going to infinity can be treated analytically by using the so-called 'snippet' basis [62, 63].

For strong but finite couplings, i.e. $1/g_\alpha \ll 1$, recent research also unveiled the existence of a mapping to an effective spin-chain model by employing perturbation theory with respect to the 'snippet' basis. Various intriguing ground-state configurations have been revealed depending on the ratio and the sign of the interaction parameters: Heisenberg antiferromagnet (AFM)/ferromagnet (FM), Ising AFM/FM and XY phase [64–68]. Such a mapping is applicable not only for Bose–Bose mixtures, but also Bose–Fermi and Fermi–Fermi mixtures may be treated with this approach.

The last case we discuss is the highly asymmetric case $g_A = 0$ and $g_B = 100$ in figure 1(e). For $g_{AB} = 0$ (BEC-TG) one expects, based on the previous considerations, integer eigenvalues $E_{0,k,l,m}^{(0)} \approx k + 2l + 2m + 3$ and thus equal spacings as for the cases $g_\sigma = 0$ and $g_\sigma = 100$ depicted in figures 1(a) and (d), because the PCF of the A component is an even HO eigenstate and the PCF of the B component is degenerate with an odd HO eigenstate. Very peculiar is the strong coupling case, where we observe a non-degenerate ground state, the so-called PS phase [40], where the A component occupies the centre of the harmonic trap, while the B component, in order to reduce its intra-component interaction energy, forms a shell around the A component.

4.3. Relative-frame densities

Let us now inspect the relative-frame probability densities $\rho_1(Y_i)$ instead of the usually studied one-body densities $\rho_1(x_\sigma)$ of the laboratory frame as e.g. in [40]. We will see that these quantities can be used to identify regions of most probable relative distances and provide a more detailed picture of particle arrangements than their laboratory frame counterparts. Moreover, in the quench dynamics study, the subject of the next section, an occupation of a certain eigenstate of H will lead to the breathing oscillation of only one relative-frame density, making it possible to connect different breathing modes to specific relative motions within the system, at least for the weakly coupled case $g_{AB} \ll 1$.

We define these quantities as follows:

$$\rho_1^{(j)}(Y_i) = \int \prod_{p \neq i} dY_p \; |\langle \vec{Y} | E_j \rangle|^2, \tag{12}$$

where $|E_j\rangle$ is the jth eigenstate of H and we trace out all the degrees of freedom of the relative frame $\vec{Y}$ except for one.
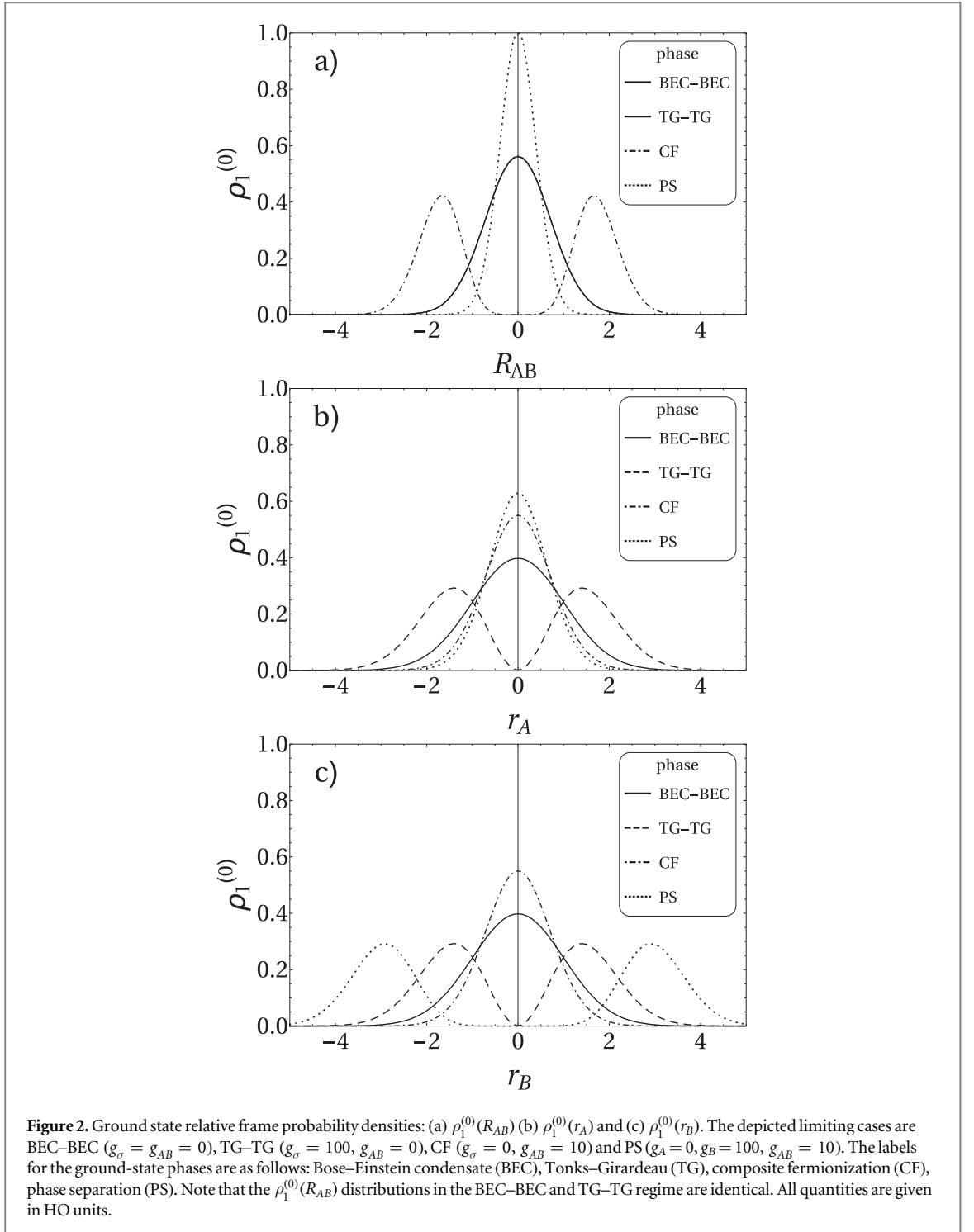
Let us compare our results concerning the ground state densities for some limiting cases to the ones obtained in [40]. In figure 2 we show the densities for all the degrees of freedom except for R_{CM}, which trivially obeys a Gaussian distribution. In the BEC–BEC case all the densities are characterized by a Gaussian density profile, since the Hamiltonian consists of completely decoupled HOs for each degree of freedom.

When the g_{AB} coupling is turned off, the ground state is known analytically: $\Phi_0^{AB}(R_{AB}) \varphi_{\mu(g_A,0)}^A(r_A) \varphi_{\mu(g_B,0)}^B(r_B)$. Thus, by tracing out the r_σ coordinates we acquire the same $\rho_1^{(0)}(R_{AB})$ for arbitrary intra-component interactions, which explains the identical distributions for the BEC–BEC and TG–TG phase in figure 2(a). While the PCF $\varphi_{\mu(g_\sigma,0)}^\sigma(r_\sigma)$ is identical to the HO ground state for $g_\sigma = 0$, for any finite positive g_σ it splits into two symmetric peaks with a cusp at the origin, which tends to zero as $g \to \infty$ [57]. In this limit it becomes equivalent to the modulus of the first excited HO eigenstate, which explains the shape of the TG-curves in figures 2(b), (c). We remark that going beyond $g_\sigma = 100$ does not induce substantial changes on the densities, which justifies our interpretation of this parameter regime as TG limit.

The CF phase is in some sense a complete counter-part to the TG–TG case. Now $\rho_1^{(0)}(R_{AB})$ features two maxima and a minimum in between, a result of A and B strongly repelling each other. This feature is blurred in the one-body density distributions $\rho_1^{(0)}(x_\sigma)$ of the laboratory frame and one needs to additionally consider the two-body density function $\rho_2^{(0)}(x_A, x_B)$ to verify this behaviour [37]. The density distribution of $\rho_1^{(0)}(r_\sigma)$ is more compressed compared to the BEC–BEC case due to the tighter confinement induced by the other component.

Finally, the PS phase corresponds to a core–shell structure, where $\rho_1^{(0)}(R_{AB})$ and $\rho_1^{(0)}(r_A)$ show a more pronounced peak, while $\rho_1^{(0)}(r_B)$ obeys a bimodal distribution with two density peaks being much further apart than both in the CF and in the TG–TG case. This can be understood in the following way: firstly, the fact that A locates in the trap centre and not the other way around is because B needs to minimize its repulsive intra-component interaction energy by separating its particles. Secondly, the need to minimize the repulsive inter-component energy pushes the B particles even further along the harmonic trap at the cost of increased potential energy until these two energies balance themselves out. The two A particles are compressed to closer distances as compared to the BEC–BEC case because of a tighter trap induced by B, while at the same time A modifies the HO

Figure 2. Ground state relative frame probability densities: (a) $\rho_1^{(0)}(R_{AB})$ (b) $\rho_1^{(0)}(r_A)$ and (c) $\rho_1^{(0)}(r_B)$. The depicted limiting cases are BEC–BEC ($g_\sigma = g_{AB} = 0$), TG–TG ($g_\sigma = 100$, $g_{AB} = 0$), CF ($g_\sigma = 0$, $g_{AB} = 10$) and PS ($g_A = 0$, $g_B = 100$, $g_{AB} = 10$). The labels for the ground-state phases are as follows: Bose–Einstein condensate (BEC), Tonks–Girardeau (TG), composite fermionization (CF), phase separation (PS). Note that the $\rho_1^{(0)}(R_{AB})$ distributions in the BEC–BEC and TG–TG regime are identical. All quantities are given in HO units.

potential to a double well for *B*. This results in stronger localization of particles, which leads to a more pronounced peak in the R_{AB} distribution.

5. Breathing dynamics

The spectral properties discussed above can be probed by slightly quenching a system parameter such that the lowest lying collective modes are excited. Here, we focus on a slight quench of the trapping frequency in order to excite the breathing or monopole modes being characterized by a periodic expansion and compression of the atomic density. While in the single-component case two lowest lying breathing modes of in general distinct frequencies exist, being associated with a motion of the CM and the relative coordinates [24, 43], respectively,

the number of breathing modes, their frequencies and the associated 'normal coordinates'[7] are so far unknown for the more complex case of a binary few-body mixture and shall be the subject of this section.

Experimentally, breathing oscillations can be studied by measuring the width of the σ species density distribution $\int dx_\sigma \, x_\sigma^2 \rho_1(x_\sigma, t)$ where we have omitted the subtraction of the mean value $\int dx_\sigma \, x_\sigma \rho_1(x_\sigma, t)$ squared, which vanishes due to the parity symmetry. From a theoretical point of view, it is fruitful to define a breathing observable as $\sum_{\sigma,i} x_{\sigma,i}^2$, whose expectation value is essentially the sum of the widths of the A and the B component.

To study the breathing dynamics we will perform a slight and component-symmetric quench of the HO trapping frequency, where our HO units will be given with respect to the post-quench system. The initial state for this quench scenario is the ground state $|\Psi(t = 0)\rangle = |E_0\rangle_{\omega_0}$ of the pre-quench Hamiltonian $H(\omega_0)$ with harmonic trapping frequency $\omega_0 \gtrsim 1$, where $H(\omega_0)$ is obtained from equation (1) by multiplying the harmonic potential terms with the pre-factor ω_0^2. At time $t = 0$ a sudden quench is performed to $\omega = 1$. The time evolution is thus governed by the post-quench Hamiltonian H (see equation (1)) as follows:

$$|\Psi(t)\rangle = e^{-iHt}|E_0\rangle_{\omega_0} \approx \sum_{j=0}^{n} c_j e^{-iE_j t}|E_j\rangle, \tag{13}$$

where $|E_j\rangle \equiv |E_j\rangle_\omega$ and $c_j = \langle E_j|E_0\rangle_{\omega_0}$ is the overlap between the initial state and the jth eigenstate $|E_j\rangle$ of the post-quench Hamiltonian H. Since both the pre- and post-quench Hamiltonian are time-reversal symmetric, we assume their eigenstates and thereby also the overlap coefficients c_j to be real-valued without loss of generality. A small quench ensures that $|c_0| \approx 1$ and only the n lowest excited states are of relevance. Symmetry considerations further reduce the number of allowed contributions. E.g. states of odd R_{CM}-parity or odd R_{AB}-parity have zero overlap with $|E_0\rangle_{\omega_0}$, because the initial state is of even R_{CM}- and R_{AB}-parity and the quench does not affect any of the symmetries discussed in the previous section. Similarly, in the component-symmetric case $g_A = g_B$, states, which are antisymmetric w.r.t. the S_r operation, have no overlap with the pre-quench ground state being symmetric under S_r.

For the weakly coupled regime, the relative-frame coordinates turn out to be extremely helpful for characterizing the participating breathing modes. Therefore, we study in particular the reduced densities of the relative-frame coordinates. Employing the expansion in post-quench eigenstates from equation (13), their time-evolution may be approximated within the linear-response regime as

$$\rho_1(Y_i, t) \approx c_0^2 \rho_1^{(0)}(Y_i) + 2\sum_{j=1}^{n} c_0 c_j \rho_1^{(0,j)}(Y_i)\cos(\Delta_j t), \tag{14}$$
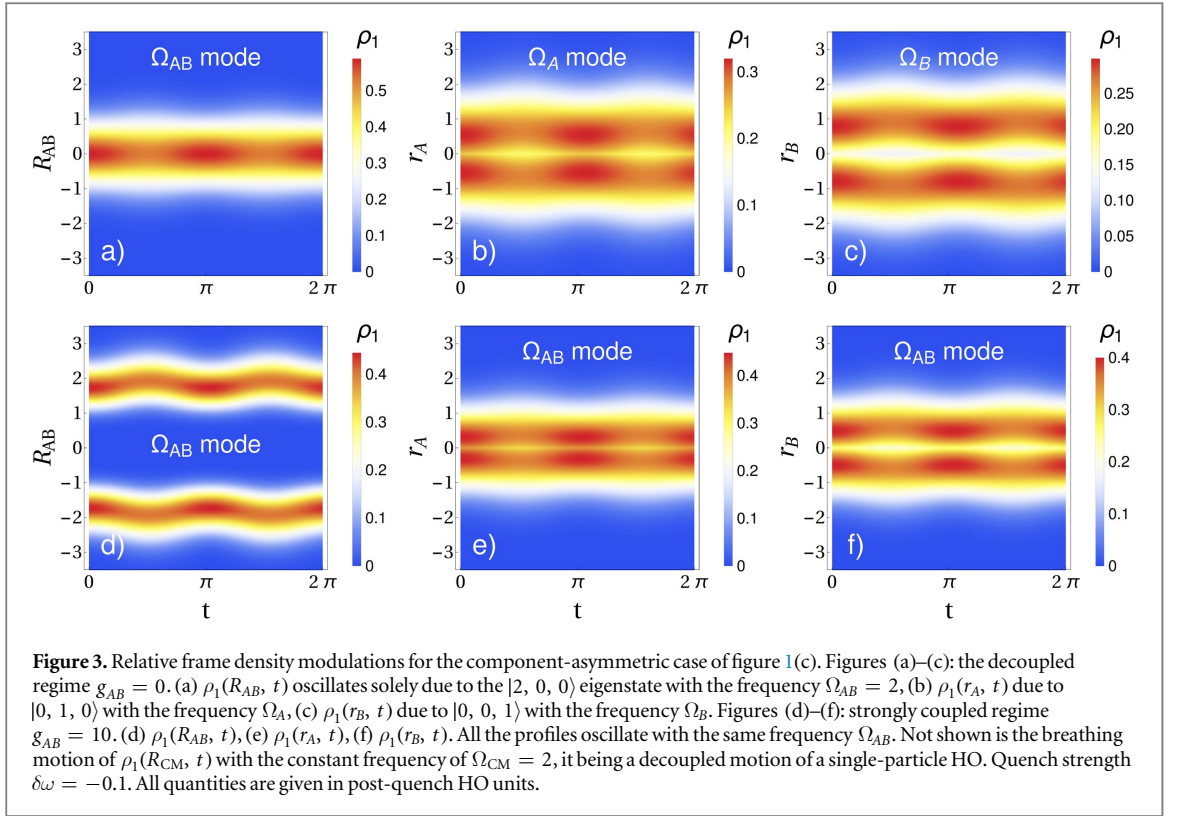
neglecting terms of the order $c_i c_j$ for $i, j > 0$. So $\rho_1(Y_i, t)$ can be decomposed into the stationary background $\rho_1^{(0)}(Y_i)$ and time-dependent modulations of the form $\rho_1^{(0,j)}(Y_i) = \int \prod_{p \neq i} dY_p \, \langle \vec{Y}|E_0\rangle \langle E_j|\vec{Y}\rangle$, further called transition densities, with oscillation frequency $\Delta_j = E_j - E_0$. Below we discuss how to calculate the overlaps c_j (see equations (18), (19)) to a good approximation only in terms of the post-quench Hamiltonian eigenstates for sufficiently weak quenches. Thus, we can fully simulate the time-evolution of $\rho_1(Y_i, t)$ by using only the post-quench Hamiltonian properties obtained in section 4.

In the following, we regard the excitations of the first even R_{AB}-parity branch as the lowest monopole modes and show that each monopole mode is directly connected to the breathing modulation of a single relative-frame density, if the two components are but weakly coupled. This behaviour changes for increasing g_{AB}, where each coordinate begins to exhibit an oscillation with more than one frequency. By inspecting the modulations of the variances of each relative-coordinate and taking the excitation amplitudes into account, we show that four (three) breathing modes are excited for $g_A \neq g_B$ ($g_A = g_B$) in the weakly coupled regime, while only two breathing modes are of relevance in the strongly coupled regime. First, we inspect the component-asymmetric case of figure 1(c) in detail to illustrate some peculiarities of the involved breathing modes, since it contains the most relevant features. Thereafter, we unravel differences to the component-symmetric case of figure 1(b).

5.1. Component-asymmetric case

Because of the low amplitude quenching protocol, we will excite four breathing modes simultaneously in the component-asymmetric case ($g_A = 1$, $g_B = 2$). Three of them stem from the first even R_{AB}-parity branch of figure 1(c). Remember, however, that the total CM was assumed to be in the ground state to keep the spectrum discernible. One obtains the full energy spectrum by including all CM excitations, meaning duplicating and up-shifting depicted energy curves by $\Delta E = n$ with $n \in \mathbb{N}$. This reveals a forth mode, namely a double total CM excitation. It features the same parity symmetries and is energetically of the same order as the states from the first even R_{AB}-parity branch ensuring a considerable overlap with the initial state. The total CM trivially oscillates

---

[7] In this work, we call coordinates normal if they completely decouple the Hamiltonian, implying the possibility to excite each degree of freedom independently.

Figure 3. Relative frame density modulations for the component-asymmetric case of figure 1(c). Figures (a)–(c): the decoupled regime $g_{AB} = 0$. (a) $\rho_1(R_{AB}, t)$ oscillates solely due to the $|2, 0, 0\rangle$ eigenstate with the frequency $\Omega_{AB} = 2$, (b) $\rho_1(r_A, t)$ due to $|0, 1, 0\rangle$ with the frequency Ω_A, (c) $\rho_1(r_B, t)$ due to $|0, 0, 1\rangle$ with the frequency Ω_B. Figures (d)–(f): strongly coupled regime $g_{AB} = 10$. (d) $\rho_1(R_{AB}, t)$, (e) $\rho_1(r_A, t)$, (f) $\rho_1(r_B, t)$. All the profiles oscillate with the same frequency Ω_{AB}. Not shown is the breathing motion of $\rho_1(R_{CM}, t)$ with the constant frequency of $\Omega_{CM} = 2$, it being a decoupled motion of a single-particle HO. Quench strength $\delta\omega = -0.1$. All quantities are given in post-quench HO units.

with the constant frequency $\Omega_{CM} = 2$ independent of any interactions g_α it being a decoupled degree of freedom with the single-particle HO Hamiltonian (equation (5)) [25, 43]. The other three modes, which are excited, are known analytically, when there is no coupling between the components, and we label the corresponding mode frequencies as (see also the labels in figure 1(c)):

(i) $|0\rangle|0, 1, 0\rangle$ $\leftrightarrow$ $\Omega_A(g_{AB} = 0) = \mu(g_A, 1) - \mu(g_A, 0)$,

(ii) $|0\rangle|0, 0, 1\rangle$ $\leftrightarrow$ $\Omega_B(g_{AB} = 0) = \mu(g_B, 1) - \mu(g_B, 0)$,

(iii) $|0\rangle|2, 0, 0\rangle$ $\leftrightarrow$ $\Omega_{AB}(g_{AB} = 0) = 2$,

(iv) $|2\rangle|0, 0, 0\rangle$ $\leftrightarrow$ $\Omega_{CM} = 2$,

where we have prepended the CM eigenstate $|n\rangle$ for a complete characterization of the involved states. States of higher order even R_{AB}-parity branches as well as higher excitations of the CM coordinate are negligible due to small overlaps with the initial state.

In the uncoupled regime $g_{AB} = 0$, one can show analytically that each relative-coordinate density oscillates with a single frequency, each corresponding to exactly one eigenstate of the first even R_{AB}-parity branch (see figures 3(a)–(c)). E.g. for $\rho_1(R_{AB}, t)$, the only transition density $\rho_1^{(0,j)}(R_{AB})$ which survives taking the partial trace is the one corresponding to $|0\rangle|2, 0, 0\rangle$, while the contributions from the remaining excited states vanish. This leads to the breathing motion in the R_{AB} coordinate with a single frequency Ω_{AB}. Analogously one can show that $|0\rangle|0, 1, 0\rangle$ solely induces density modulation in $\rho_1(r_A)$ with the frequency Ω_A, while $\rho_1(r_B)$ oscillates with Ω_B exclusively due to $|0\rangle|0, 0, 1\rangle$. Thereby, the relative-frame coordinates render 'normal coordinates' in the uncoupled regime, which is also a valid picture for extremely weak couplings.

By introducing a larger coupling between the components one observes that each relative frame density, except for $\rho_1(R_{CM}, t)$, begins to oscillate with up to three frequencies simultaneously. So all the modes begin to contribute to the density modulation of each relative coordinate. However, there are some peculiarities we observe, for the visualization of which the densities are not well suited any more. Instead, we will transform the breathing observable to the relative frame and consider the expectation values of individual terms it decomposes into:

$$\sum_{\sigma, i} x_{\sigma, i}^2 = 4R_{CM}^2 + R_{AB}^2 + \frac{1}{2}r_A^2 + \frac{1}{2}r_B^2. \tag{15}$$

The expectation value of each observable with respect to the time-evolved state $|\Psi(t)\rangle$ is directly related to the respective relative-frame density:

$$\langle \Psi(t)|Y_i^2|\Psi(t)\rangle = \int dY_i \; Y_i^2 \; \rho_1(Y_i, t). \tag{16}$$

Inserting the time-evolution of the relative frame density from equation (14) one finds that the observables decompose into a stationary value and a time-dependent modulation as well. In particular, we are interested in the amplitudes of modulations, when the inter-component coupling is varied, since they determine how many frequencies are of essential relevance for the considered motion. The amplitude of the jth mode is essentially composed of the overlap c_j and of the transition element:

$$\langle E_j|Y_i^2|E_0\rangle = \int dY_i \; Y_i^2 \; \rho_1^{(0,j)}(Y_i). \tag{17}$$

In order to evaluate the overlaps $c_j = \langle E_j|E_0\rangle_{\omega_0}$ with $j \neq 0$ in terms of only the post-quench Hamiltonian eigenstates, we perform a Taylor approximation with respect to the weak quench strength $\delta\omega = \omega - \omega_0$, namely $|E_0\rangle_{\omega_0} \approx |E_0\rangle_\omega - \delta\omega \frac{d}{d\omega}|E_0\rangle_\omega$ evaluated at $\omega = 1$, and arrive at

$$c_j \approx -\left\langle E_j \left| \frac{d}{d\omega} \right| E_0 \right\rangle \delta\omega. \tag{18}$$

Applying the (off-diagonal) Hellmann–Feynman theorem [69], one obtains:

$$\left\langle E_j \left| \frac{d}{d\omega} \right| E_0 \right\rangle = \frac{-\omega \left\langle E_j \left| \sum_{i,\sigma} x_{i,\sigma}^2 \right| E_0 \right\rangle}{E_j - E_0}. \tag{19}$$

The overlaps are hence connected to the transition elements of each relative-frame breathing observable (equation (15)), weighted with the inverse of the mode frequency, which leads to a damping of contributions from higher order branches. This relation enables us to calculate the amplitude A_j, with which the jth mode contributes to the oscillation of the observable Y_i^2:
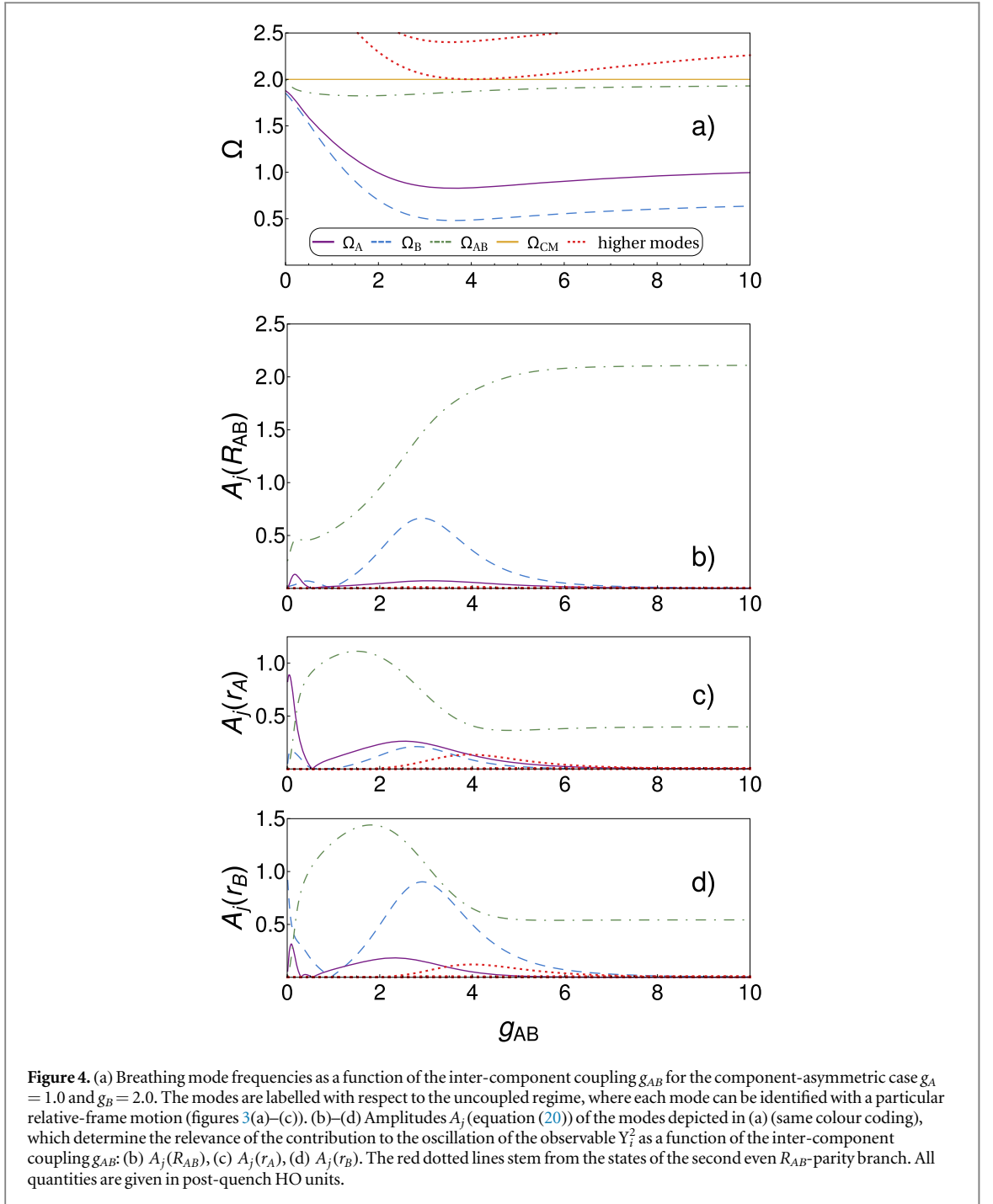
$$A_j(Y_i) = \left| \frac{c_j}{\delta\omega} \langle E_j|Y_i^2|E_0\rangle \right|, \tag{20}$$

which may be interpreted as the susceptibility of the Y_i^2 observable for the excitation of the state $|E_j\rangle$.

In figure 4(a) we show the values of possible breathing mode frequencies, obtained from the spectrum of figure 1(c). $\Omega_{CM} = 2$ does not depend on any interaction strength g_α. In contrast to this, Ω_{AB} is degenerate with Ω_{CM} for $g_{AB} = 0$, and when increasing g_{AB}, decreases to a minimum first and then increases with the tendency to asymptotically reach Ω_{CM} again. This behaviour strongly resembles the dependence of the relative-coordinate breathing-mode frequency in the single-component case [43]. Ω_A and Ω_B have qualitatively akin curve shapes, varying much stronger with g_{AB}. In particular, we note that these frequencies reach values below the frequency of the CM dipole mode being equal to unity.

The breathing mode frequencies discussed above are labelled according to the peculiarity of the uncoupled regime, where each eigenstate from the first even R_{AB}-parity branch leads to a breathing motion of some specific relative-frame coordinate. Indeed, if we look at the amplitudes A_j in figures 4(b)–(d) in the decoupled regime ($g_{AB} = 0$), we recognize that the amplitude for the coordinate Y_i is non-zero only for one mode, namely the one with which $\rho_1(Y_i, t)$ oscillates in figures 3(a)–(c). When we increase the inter-component coupling, the eigenstates cease to be simple product states in the relative coordinate frame resulting in contamination of each density modulation with the frequencies from the other modes as well, which leads to a three-mode oscillation. Nevertheless, we label the frequencies corresponding to the uncoupled case and follow the states continuously throughout the g_{AB} variation.
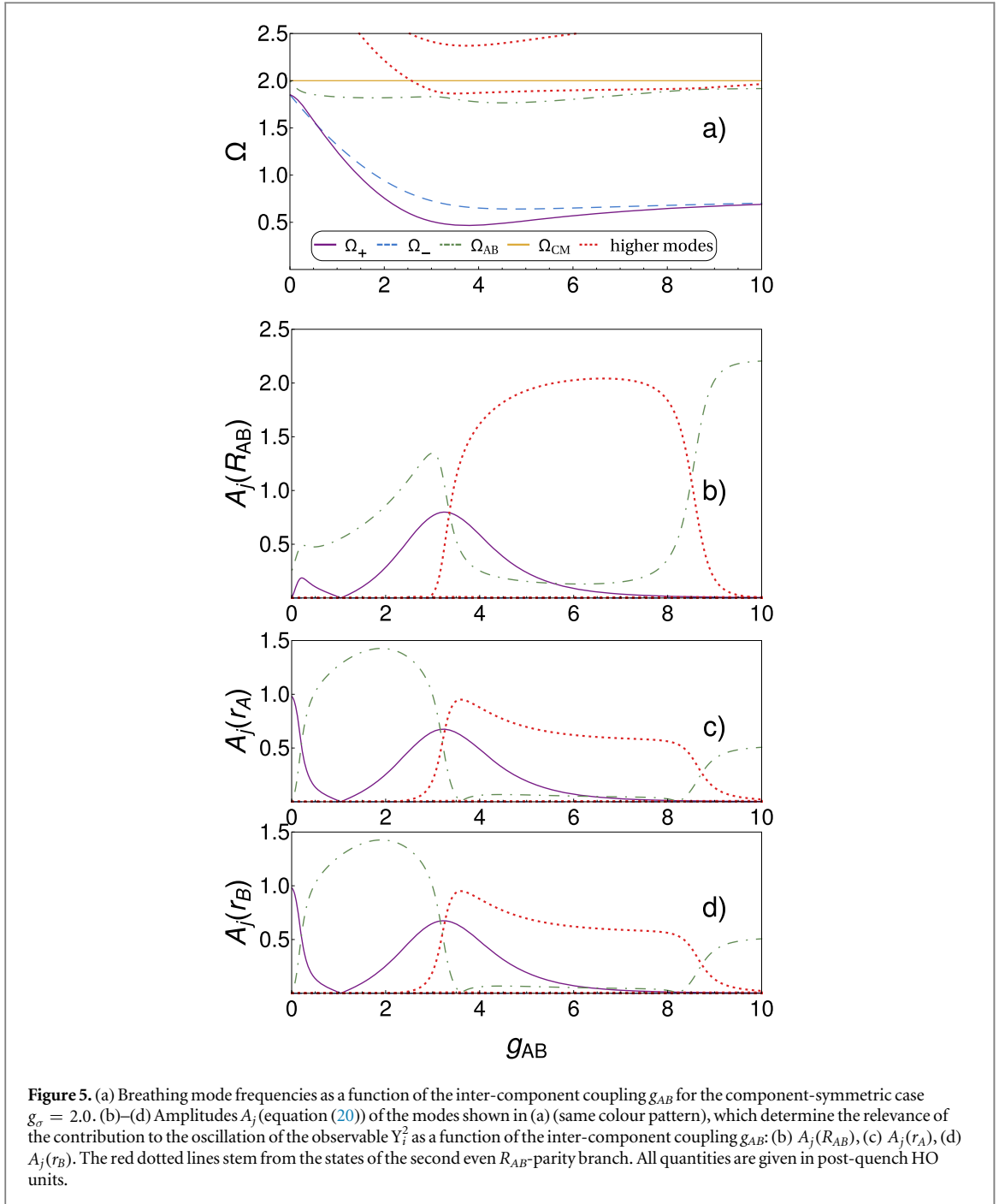
Another peculiarity worth noting arises in the strongly coupled regime: The Ω_σ oscillations become strongly suppressed for all the observables making Ω_{AB} and Ω_{CM} the main contributors to the density modulations, which reminds us of the single-component behaviour [43]. Furthermore, the dependence of Ω_{AB} on g_{AB} has striking resemblance to the dependence of Ω_{rel} on g for the single component gas. In figures 3(d)–(f) we show that all the relative-coordinate densities oscillate with the same frequency Ω_{AB}. We highlight that in the CF regime each density peak of the bimodal distribution $\rho_1(R_{AB}, t)$ does not only breath periodically but also its maximum height position performs dipole-mode like oscillations, see figure 3(d). Our intuitive picture for this effect is as follows: in the CF phase the two species are located on opposite sides of the HO trap and feel a tighter effective trap induced by the other component, which is in accordance to the tighter localization of the r_σ coordinates, see figures 2(b) and (c). Upon inducing the quench dynamics by instantly lowering the trap frequency, the two species separate even further. When the turning point is reached, they move back towards the centre of the trap, fail, however, to penetrate each other due to a strong mutual repulsion, which results in dipole-like oscillation of each of the two $\rho_1(R_{AB}, t)$ density fragments. These dipole oscillations quite likely act as

Figure 4. (a) Breathing mode frequencies as a function of the inter-component coupling g_{AB} for the component-asymmetric case $g_A = 1.0$ and $g_B = 2.0$. The modes are labelled with respect to the uncoupled regime, where each mode can be identified with a particular relative-frame motion (figures 3(a)–(c)). (b)–(d) Amplitudes A_j (equation (20)) of the modes depicted in (a) (same colour coding), which determine the relevance of the contribution to the oscillation of the observable Y_i^2 as a function of the inter-component coupling g_{AB}: (b) $A_j(R_{AB})$, (c) $A_j(r_A)$, (d) $A_j(r_B)$. The red dotted lines stem from the states of the second even R_{AB}-parity branch. All quantities are given in post-quench HO units.

a driving force for the r_σ coordinates making them to oscillate with the same frequency thereby suppressing Ω_σ modes.

5.2. Component-symmetric case

Now we compare the above results with the component-symmetric case of figure 1(b), where $g_A = g_B = 2$. Figure 5(a) depicts the possible breathing-mode frequencies. Here, two main differences arise: first, the Ω_{AB} curve features two minima due to two avoided crossings with an eigenstate of the second even R_{AB}-parity branch. Second, the other two breathing mode frequencies of the relative coordinates are degenerate for $g_{AB} = 0$, then separate with increasing g_{AB} and approach one another asymptotically. Instead of using the labels Ω_A and Ω_B as in the component-asymmetric case, we label these two modes with Ω_+ and Ω_-, since the corresponding excited eigenstates are symmetric and antisymmetric w.r.t. S_r, respectively (see figure 1(b)). The latter frequency, however, does not give any contribution to the breathing dynamics, it being symmetry excluded.

Figure 5. (a) Breathing mode frequencies as a function of the inter-component coupling g_{AB} for the component-symmetric case $g_{\sigma} = 2.0$. (b)–(d) Amplitudes A_j (equation (20)) of the modes shown in (a) (same colour pattern), which determine the relevance of the contribution to the oscillation of the observable Y_i^2 as a function of the inter-component coupling g_{AB}: (b) $A_j(R_{AB})$, (c) $A_j(r_A)$, (d) $A_j(r_B)$. The red dotted lines stem from the states of the second even R_{AB}-parity branch. All quantities are given in post-quench HO units.

The motion of the r_A and r_B coordinates is identical due to the imposed component-symmetry and in the uncoupled regime ($g_{AB} = 0$) they both oscillate solely with the Ω_+ frequency (see figures 5(c) and (d)). Similarly to the component-asymmetric case, we see that when increasing g_{AB} the Ω_{AB} (Ω_+) mode contributes also to the observable r_{σ}^2 (R_{AB}^2).

However, in the intermediate interaction regime $3.7 \lesssim g_{AB} \lesssim 8.3$ we observe a strong suppression of the Ω_{AB} mode contribution for all observables, which is in stark contrast to the component-asymmetric case. Instead, a state of the second even R_{AB}-parity branch gains relevance. These two eigenstates actually participate in the avoided crossing exemplary indicated by an arrow in the spectrum (see figure 1(b)) and thereby exchange their character. According to equation (20) the breathing amplitude is determined by the transition elements (16) as well as the overlap coefficients (18), which in turn depend also on the transition elements due to equations (19) and (15). While the energy denominator of equation (19) does not single out one of the two states participating in the avoided crossing, the values of the individual transition elements strongly depend on the character of the respective eigenstate. Thereby, the energetically slightly lower mode has a large amplitude before the crossing and after the crossing the composition character of states changes such that the higher mode dominates. By further increasing g_{AB} we observe another exchange of roles, which is attributed to the presence of

a second avoided crossing (see figure 5(a)) such that the strong inter-component coupling regime shows again the absolute dominance of the Ω_{AB} mode over the other lowest breathing modes besides Ω_{CM}.

6. Experimental realization

The few-body Bose–Bose mixture studied here should be observable with existing cold atom techniques. Quantum gas microscopes allow the detection of single particles in a well controlled many-body or few-body system [70, 71] and recent progress also allows for spin-resolved imaging in 1D systems using an expansion in the perpendicular direction [72, 73]. In these set-ups, the single-particle sensitivity relies on pinning the atoms in a deep lattice during imaging and experiments have so far focused on lattice systems. However, bulk systems might be imaged with high spatial resolution by freezing the atomic positions in a lattice before imaging. For fast freezing, this would allow a time-resolved measurement of the breathing dynamics. Moreover, spin order was recently observed in very small fermionic bulk systems via spin-selective spilling to one side of the system [74].

Deterministic preparation of very small samples was demonstrated for fermions via trap spilling [75] and for bosons by cutting out a subsystem of a Mott insulator [76]. The tight transverse confinement for a 1D system can be obtained from a 2D optical lattice, while the axial confinement would come from an additional optical potential, which can be separately controlled to initialize the breathing mode dynamics.

Choosing two hyperfine states of the same atomic species ensures the same mass of the two bosonic species. Possible choices include ^{7}Li, ^{39}K or ^{87}Rb. While the former have usable FRs to tune the interaction strengths, the latter allows selective tuning via CIR in a spin-dependent transversal confinement as can be realized for heavier elements. Note that the longitudinal confinement needs to be spin-independent in order to ensure the same longitudinal trap frequencies and trap centres assumed in the calculations. The inter-component interaction strength can be tuned via a transverse spatial separation as obtained e.g. from a magnetic field gradient [77]. In the case of ^{7}Li and ^{39}K, the inter-component background scattering lengths are negative [14] leading to negative g_{AB}, but although not reported, inter-component FRs might exist. Alternatively, g_{AB} might be tuned via a CIR, which selectively changes g_{AB} at magnetic fields, where the intra-component scattering lengths are very different.

In the following we give concrete numbers for a choice of ^{7}Li. The density distribution has structures on the scale of the HO unit a_{ho} (figure 2). Choosing the trap parameters as in [75] as $\omega/(2\pi) = 1.5\,$kHz and $\omega_\perp/(2\pi) = 15\,$kHz, yields $a_{ho} = 1\,\mu$m, i.e. larger than a typical optical resolution of 0.8 μm. At the same time, temperatures much lower than $\hbar\omega/k_B = 72\,$nK are state of the art. The breathing dynamics will occur on a time scale of several 100 μs, which is easily experimentally accessible. Choosing a smaller ω would make the imaging easier, but would impose stricter requirements on the temperature.

For the observation of the breathing mode dynamics, one would record the positions of all four particles in each experimental image and obtain the widths $\langle R_{CM}^2 \rangle_t$, $\langle R_{AB}^2 \rangle_t$, $\langle r_\sigma^2 \rangle_t$ by averaging the occurring relative coordinates over many single-shots after a fixed hold time t.

7. Discussion and outlook

In this work we have explored a few-body problem of a Bose-Bose mixture with two atoms in each component confined in a quasi-1D HO trapping potential by exact diagonalization. By applying a coordinate transformation to a suitable frame we have constructed a rapidly converging basis consisting of HO and PCF. The latter stem from the analytical solution of the relative part of the two-atom problem [57] and include the information about the intra-species correlations, which renders our basis superior to the common approach of using HO eigenstates as basis states.

We have then explored the behaviour of the low-lying energy spectrum as a function of the inter-species coupling for various fixed values of intra-species interaction strengths. Hereby we have covered the strongly coupled limiting cases of CF, FF and PS, studied also intermediate symmetric and asymmetric values of g_A and g_B and related the ground state relative-frame densities of some limiting cases to the known laboratory frame results [40]. We have discussed the evolution of degeneracies and explained appearing (avoided) crossings in terms of the symmetries of the Hamiltonian, which become directly manifest in the chosen relative-coordinate frame.

Finally, the obtained results were used to study the dynamics of the system under a slight component-symmetric quench of the trapping potential. We have derived expressions for the time evolution of the relative-frame densities within the linear response regime and observed that in the uncoupled regime ($g_{AB} = 0$) the density of each relative frame coordinate performs breathing oscillations with a single frequency corresponding to a specific excited state of the first even R_{AB}-parity branch of the spectrum. The total CM coordinate performs breathing oscillations with the frequency $\Omega_{CM} = 2$ (HO units). For *asymmetric* choices of g_σ values, three

additional monopole modes participate in the dynamics, each of them corresponding to the motion of a particular relative coordinate: Ω_A for the relative coordinate of the A component, Ω_B for the relative coordinate of the B component and Ω_{AB} for the relative distance of the CMs of both components. In contrast to this, the *symmetric* case $g_A = g_B$ leads to only two additional modes because of a symmetry-induced selection rule: Ω_+ for the relative coordinates of both components and Ω_{AB} for the relative distance of the CMs of both components.

For not too strong inter-component coupling, each relative coordinate exhibits multi-mode oscillations and we have explored their relevance for the density modulations by analysing the behaviour of suitably chosen observables as one gradually increases the coupling between the components for symmetric and asymmetric choices of intra-component interactions strengths. Thereby, we have found that for strong couplings, where CF takes place, the Ω_σ (Ω_+) modes become highly suppressed, leaving only two monopole modes in this regime: Ω_{AB} and Ω_{CM}. We have observed the same effect for the case of PS (results not shown). Interestingly, the dependence of Ω_{AB} on g_{AB} strongly resembles the behaviour of the relative-coordinate breathing frequency in the single-component case [43]. All in all, we have obtained 2 to 4 monopole modes for the quench dynamics depending on the strength of the inter-component coupling and the symmetry of the intra-species interactions, which is in strong contrast to the single-component case [43] as well as to the MF results, where two low-lying breathing modes can be obtained, namely an in-phase (out-of-phase) mode for a component-symmetric (component-asymmetric) quench [23]. Finally, we have argued that the experimental preparation of the considered few-body mixture and measurement of the predicted effects are in reach by means of state-of-the-art techniques.

This work serves as a useful analysis tool for future few-body experiments. Measurements of the monopole modes can be mapped to the effective interactions within the system such that precise measurements of the scattering lengths or external magnetic fields can be performed. The numerical method used here can be applied to Bose–Fermi and Fermi–Fermi mixtures with two particles in each component simplifying the numerics, because the PCFs have to be replaced by odd HO eigenstates, if a bosonic component is switched to a fermionic one, which significantly accelerates the calculation of integrals. Further, it would be interesting to see how the frequencies and the amplitudes of the monopole modes vary for an increasing number of particles. Exploring the spectrum for negative values of interaction parameters is also a promising direction of future research.

Acknowledgments

Appendix

In the following, we discuss how to efficiently calculate matrix elements of the coupling operator H_1 from equation (8) with respect to the basis (10). Because of the already mentioned even parity of φ_i^σ one can make simple substitutions of the form $\tilde{r}_\sigma = -r_\sigma$ to show that each delta in the sum of H_1 gives the same contribution, such that after performing an integral over R_{AB} one obtains:

$$\langle a,\, b,\, c | H_1 | k,\, l,\, m \rangle = 4 \int \mathrm{d}r_A \int \mathrm{d}r_B \; \Phi_a^{AB}\left(\frac{r_A + r_B}{2}\right) \Phi_k^{AB}\left(\frac{r_A + r_B}{2}\right)$$
$$\times \; \varphi_b^A(r_A)\, \varphi_l^A(r_A)\, \varphi_c^B(r_B)\, \varphi_m^B(r_B). \tag{A1}$$

At this point it is important to notice that the integral vanishes for odd $(a + k)$ because of the parity symmetries of Φ^{AB} and φ^σ, which can be seen by transforming to relative and centre-of-mass coordinates $r = r_A - r_B$, $R = (r_A + r_B)/2$. In the following, we assume that the quantum numbers for the R_{AB} coordinate are restricted to $a,\, k \in \{1, \ldots, n_{AB}\}$ and for the r_σ coordinates to $b,\, c,\, l,\, m \in \{1, \ldots, n_{rel}\}$. Now our computation strategy consists of three steps:

First, we circumvent evaluating the 2D integral from equation (A1) by viewing the product of the two HO eigenstates $\Phi_a^{AB}\Phi_k^{AB}$ as a pure, in general not normalized state $\chi_{a,k}$ depending on the two coordinates r_A and r_B and applying the Schmidt decomposition [58] or, equivalently, the so-called POTFIT algorithm [59].

$$\chi_{a,k}(r_A, r_B) \equiv \Phi_a^{AB}\left(\frac{r_A + r_B}{2}\right)\Phi_k^{AB}\left(\frac{r_A + r_B}{2}\right)$$

$$\approx \sum_{i=0}^{d} \lambda_i^{(a,k)} w_i^{A;(a,k)}(r_A) w_i^{B;(a,k)}(r_B). \tag{A2}$$

Here[8], $|\lambda_i^{(a,k)}|^2$ coincides with the ith eigenvalue of the reduced one-body density matrix corresponding to the degree-of-freedom r_σ and $w_i^{\sigma;(a,k)}(r_\sigma)$ denotes the corresponding eigenvector, which can be shown to feature a definite parity symmetry. We remark that (i) we may choose $w_i^{A;(a,k)}(r) = w_i^{B;(a,k)}(r) \equiv w_i^{(a,k)}(r)$ because of $\chi_{a,k}(r_A, r_B) = \chi_{a,k}(r_B, r_A)$ without loss of generality and that (ii) the decomposition of equation (A2) becomes exact for $d \to \infty$. Having ordered the coefficients $\lambda_i^{(a,k)}$ in decreasing sequence w.r.t. to their modulus, we choose d such that only terms with $|\lambda_i^{(a,k)}/\lambda_0^{(a,k)}| > 10^{-6}$ are taken into account, which results in an accurate approximation to 2D integrals with a relative accuracy of 10^{-5}, valid for all interactions and quantum numbers considered below. We perform this decomposition for all the relevant HO quantum numbers (a, k), meaning $a \leqslant k \leqslant n_{AB}$ with $(a + k)$ even. This procedure is independent of any interactions g_α and needs to be executed only once.

By inserting equation (A2) into (A1) we obtain the following expression:

$$\langle a, b, c|H_1|k, l, m\rangle \approx 4\sum_{i=0}^{d} \lambda_i^{(a,k)} \int dr_A \; w_i^{(a,k)}(r_A)\varphi_b^A(r_A)\varphi_l^A(r_A)$$

$$\times \int dr_B \; w_i^{(a,k)}(r_B)\varphi_c^B(r_B)\varphi_m^B(r_B). \tag{A3}$$

As one can see, the 2D integral is replaced by a sum of products of 1D integrals. In order to greatly overcome the numerical effort for computing a 2D integral d should be preferably a small number (see below).

The second step consists in the calculation of 1D integrals and here we provide an efficient strategy to circumvent redundant computations. Consider the integral:

$$\int dr \; w_i^{(a,k)}(r) \; \varphi_s^\sigma(r) \; \varphi_t^\sigma(r), \tag{A4}$$

with $s \leqslant t \leqslant n_{\rm rel}$. The PCFs are of even parity and thus only even $w_i^{(a,k)}$ actually contribute allowing to reduce the number of expansion terms in equation (A3) to $\lfloor d/2 \rfloor$. Both PCFs φ_s^σ and φ_t^σ depend on the same interaction strength g_σ meaning that the above integral does not distinguish between the two subsystems such that the index σ can be dropped for the moment. Now we fix the PCFs by specifying the strength of intra-component interaction g and further we fix the HO quantum numbers (a, k), which determine the functions $w_i^{(a,k)}$, as well as PCF quantum numbers (s, t). We loop over all i and save the integral values, labelled as (g, a, k, s, t). This procedure is performed for a set I of multiple values of g we are interested in and for all the relevant quantum number configurations $a \leqslant k \leqslant n_{AB}$ with $(a + k)$ even and $s \leqslant t \leqslant n_{\rm rel}$.

In the last step we calculate the matrix elements from equation (A3). For HO quantum numbers (a, k) we extract all the expansion coefficients $\lambda_i^{(a,k)}$, obtained in the first step, and for the chosen interactions parameters (g_A, g_B) and PCF quantum numbers (b, c, l, m) we pick the appropriate integral values corresponding to $(g = g_A, a, k, s = b, t = l)$ and $(g = g_B, a, k, s = c, t = m)$. The advantage of this procedure is that not only symmetric choices of intra-component interaction strengths are accessible, but also an arbitrary asymmetric combination $(g_A, g_B) \in I \times I$. Additionally, the proposed scheme can be easily parallelized. However, adding new g values to the set I is in general very time-consuming as one needs to calculate a bunch of 1D integrals for all the relevant quantum number configurations.

Now let us analyse quantitatively the speed-up obtained by our algorithm in contrast to the straightforward evaluation of 2D integrals. Since the energy spacing of the PCF modes is approximately twice the energy spacing of the HO modes corresponding to the R_{AB} motion, we assume $n_{\rm rel} = (n_{AB} - 1)/2$ with an odd n_{AB} to keep the number of even and odd R_{AB}-parity basis states the same. The number of 1D integrals one needs to compute for each $g \in I$ in order to construct the H_1 matrix is approximately $(\bar{d}/64)[(n_{AB} + 1)(n_{AB} + 3)]^2$, where $\bar{d}$ is an average number of terms in (A3), as the criterion $|\lambda_i^{(a,k)}/\lambda_0^{(a,k)}| > 10^{-6}$ requires more terms for larger values of a, k. The number of 2D integrals amounts to $(1/256)[(n_{AB} + 1)(n_{AB} + 3)]^3$. For checking the convergence (see below), we have chosen $n_{AB} = 21$ and $n_{\rm rel} = 10$, i.e. 2662 basis states. The number of expansion terms varies in the interval $d \in \{50, \ldots, 100\}$ resulting in $\bar{d} = 75$. Thus, we need to either evaluate 326 700 1D integrals or 574 992 2D integrals. Not only is the number of 1D integrals smaller, the computation of one 2D integral takes also significantly longer than of one 1D integral, especially for higher quantum numbers. Moreover, in order to build the Hamiltonian matrix for all $(g_A, g_B) \in I \times I$, the 2D integrals (A1) would have to be evaluated for the $n_g(n_g + 1)/2$ distinct combinations $g_A \leqslant g_B$, where n_g denotes the cardinality of I, while the 1D integrals (A4) must be calculated only for all $g \in I$, i.e. n_g distinct values, which renders this approach much more efficient.

---

[8] Note that in contrast to the usual convention we do not require the coefficients $\lambda_i^{(a,k)}$ to be semi-positive without loss of generality.

For the spectra shown in section 4 we have chosen $n_{AB} = 17$ and $n_{\mathrm{rel}} = 8$, i.e. 1458 basis states. Since we know that basis states of different R_{AB}-symmetry do not couple, we can split the H matrix into subspaces of even and odd R_{AB}-parity, leading to (729×729)-size matrices for each subspace such that the computational effort for the diagonalization becomes negligible. Since the inter-component coupling g_{AB} enters the matrix $H = H_0 + g_{AB}H_1$ to be diagonalized only as a pre-factor, a very fine g_{AB} scan can be easily performed. We note that for the covered $g_{AB} \in [0, 10]$ space the convergence check provides us with the relative energy change below 1% for the low-lying energy spectrum.

References

[1] Anderson M H, Ensher J R, Matthews M R, Wieman C E and Cornell E A 1995 *Science* **269** 198
[2] Davis K B, Mewes M-O, Andrews M R, Van Druten N, Durfee D, Kurn D and Ketterle W 1995 *Phys. Rev. Lett.* **75** 3969
[3] Jin D, Ensher J, Matthews M, Wieman C and Cornell E A 1996 *Phys. Rev. Lett.* **77** 420
[4] Mewes M-O, Andrews M, Van Druten N, Kurn D, Durfee D, Townsend C and Ketterle W 1996 *Phys. Rev. Lett.* **77** 988
[5] Stringari S 1996 *Phys. Rev. Lett.* **77** 2360
[6] Myatt C, Burt E, Ghrist R, Cornell E A and Wieman C 1997 *Phys. Rev. Lett.* **78** 586
[7] Hall D, Matthews M, Ensher J, Wieman C and Cornell E A 1998 *Phys. Rev. Lett.* **81** 1539
[8] Olshanii M 1998 *Phys. Rev. Lett.* **81** 938
[9] Görlitz A *et al* 2001 *Phys. Rev. Lett.* **87** 130402
[10] Moritz H, Stöferle T, Köhl M and Esslinger T 2003 *Phys. Rev. Lett.* **91** 250402
[11] Ho T-L and Shenoy V 1996 *Phys. Rev. Lett.* **77** 3276
[12] Esry B, Greene C H, Burke J P Jr and Bohn J L 1997 *Phys. Rev. Lett.* **78** 3594
[13] Pu H and Bigelow N 1998 *Phys. Rev. Lett.* **80** 1130
[14] Chin C, Grimm R, Julienne P and Tiesinga E 2010 *Rev. Mod. Phys.* **82** 1225
[15] Papp S, Pino J and Wieman C 2008 *Phys. Rev. Lett.* **101** 040402
[16] Tojo S, Taguchi Y, Masuyama Y, Hayashi T, Saito H and Hirano T 2010 *Phys. Rev. A* **82** 033609
[17] McCarron D, Cho H, Jenkin D, Köppinger M and Cornish S 2011 *Phys. Rev. A* **84** 011603
[18] Pattinson R, Billam T, Gardiner S, McCarron D, Cho H, Cornish S, Parker N and Proukakis N 2013 *Phys. Rev. A* **87** 013625
[19] Lee K L, Jørgensen N B, Liu I-K, Wacker L, Arlt J J and Proukakis N P 2016 *Phys. Rev. A* **94** 013602
[20] Egorov M, Opanchuk B, Drummond P, Hall B, Hannaford P and Sidorov A 2013 *Phys. Rev. A* **87** 053614
[21] Pu H and Bigelow N 1998 *Phys. Rev. Lett.* **80** 1134
[22] Gordon D and Savage C 1998 *Phys. Rev. A* **58** 1440
[23] Morise H and Wadati M 2000 *J. Phys. Soc. Japan* **69** 2463
[24] Bauch S, Balzer K, Henning C and Bonitz M 2009 *Phys. Rev. B* **80** 054515
[25] Bauch S, Hochstuhl D, Balzer K and Bonitz M 2010 *J. Phys.: Conf. Ser.* **220** 012013
[26] Abraham J W, Balzer K, Hochstuhl D and Bonitz M 2012 *Phys. Rev. B* **86** 125112
[27] Abraham J and Bonitz M 2014 *Contrib. Plasma Phys.* **54** 27
[28] Menotti C and Stringari S 2002 *Phys. Rev. A* **66** 043610
[29] Haller E, Gustavsson M, Mark M J, Danzl J G, Hart R, Pupillo G and Nägerl H-C 2009 *Science* **325** 1224
[30] Fang B, Carleo G, Johnson A and Bouchoule I 2014 *Phys. Rev. Lett.* **113** 035301
[31] McDonald C, Orlando G, Abraham J, Hochstuhl D, Bonitz M and Brabec T 2013 *Phys. Rev. Lett.* **111** 256801
[32] Altmeyer A, Riedl S, Kohstall C, Wright M, Geursen R, Bartenstein M, Chin C, Denschlag J H and Grimm R 2007 *Phys. Rev. Lett.* **98** 040401
[33] Kinoshita T, Wenger T and Weiss D S 2004 *Science* **305** 1125
[34] Paredes B, Widera A, Murg V, Mandel O, Fölling S, Cirac I, Shlyapnikov G V, Hänsch T W and Bloch I 2004 *Nature* **429** 277
[35] Girardeau M 1960 *J. Math. Phys.* **1** 516
[36] Girardeau M D and Minguzzi A 2007 *Phys. Rev. Lett.* **99** 230402
[37] Zöllner S, Meyer H-D and Schmelcher P 2008 *Phys. Rev. A* **78** 013629
[38] Hao Y and Chen S 2009 *Eur. Phys. J. D* **51** 261
[39] Dehkharghani A, Volosniev A, Lindgren J, Rotureau J, Forssén C, Fedorov D, Jensen A and Zinner N 2015 *Sci. Rep.* **5** 10675
[40] García-March M A, Juliá-Díaz B, Astrakharchik G, Busch T, Boronat J and Polls A 2014 *New J. Phys.* **16** 103004
[41] García-March M A, Juliá-Díaz B, Astrakharchik G, Boronat J and Polls A 2014 *Phys. Rev. A* **90** 063605
[42] Zöllner S, Meyer H-D and Schmelcher P 2007 *Phys. Rev. A* **75** 043608
[43] Schmitz R, Krönke S, Cao L and Schmelcher P 2013 *Phys. Rev. A* **88** 043601
[44] Tschischik W, Moessner R and Haque M 2013 *Phys. Rev. A* **88** 063636
[45] Chen X-L, Li Y and Hu H 2015 *Phys. Rev. A* **91** 063631
[46] Choi S, Dunjko V, Zhang Z and Olshanii M 2015 *Phys. Rev. Lett.* **115** 115302
[47] Gudyma A I, Astrakharchik G and Zvonarev M B 2015 *Phys. Rev. A* **92** 021601
[48] Atas Y, Bouchoule I, Gangardt D and Kheruntsyan K 2017 *Phys. Rev. A* **95** 043622
[49] Koutentakis G M, Mistakidis S I and Schmelcher P 2017 *Phys. Rev. A* **95** 013617
[50] Szabo A and Ostlund N S 2012 *Modern Quantum Chemistry: Introduction to Advanced Electronic Structure Theory* (Mineola, NY: Dover Publications)
[51] Echave J and Clary D C 1992 *Chem. Phys. Lett.* **190** 225
[52] Light J C and Carrington T Jr 2007 *Adv. Chem. Phys.* **114** 263
[53] Beck M H, Jäckle A, Worth G and Meyer H-D 2000 *Phys. Rep.* **324** 1
[54] Christensson J, Forssén C, Åberg S and Reimann S M 2009 *Phys. Rev. A* **79** 012707
[55] Rotureau J 2013 *Eur. Phys. J. D* **67** 153
[56] Lindgren E, Rotureau J, Forssén C, Volosniev A and Zinner N T 2014 *New J. Phys.* **16** 063003
[57] Busch T, Englert B-G, Rzażewski K and Wilkens M 1998 *Found. Phys.* **28** 549
[58] Nielsen M A and Chuang I L 2010 *Quantum Computation and Quantum Information* (Cambridge: Cambridge University Press) p 109
[59] Jäckle A and Meyer H-D 1996 *J. Chem. Phys.* **104** 7974

[60] von Neumann J and Wigner E P 1929 *Z. Phys.* **30** 467

[61] Yukalov V and Girardeau M 2005 *Laser Phys. Lett.* **2** 375

[62] Deuretzbacher F, Fredenhagen K, Becker D, Bongs K, Sengstock K and Pfannkuche D 2008 *Phys. Rev. Lett.* **100** 160405

[63] Fang B, Vignolo P, Gattobigio M, Miniatura C and Minguzzi A 2011 *Phys. Rev.* A **84** 023626

[64] Deuretzbacher F, Becker D, Bjerlin J, Reimann S and Santos L 2014 *Phys. Rev.* A **90** 013611

[65] Volosniev A G, Petrosyan D, Valiente M, Fedorov D, Jensen A and Zinner N T 2015 *Phys. Rev.* A **91** 023620

[66] Yang L and Cui X 2016 *Phys. Rev.* A **93** 013617

[67] Deuretzbacher F, Becker D, Bjerlin J, Reimann S and Santos L 2017 *Phys. Rev.* A **95** 043630

[68] Deuretzbacher F and Santos L 2017 *Phys. Rev.* A **96** 013629

[69] Klein D and DeVries P L 1978 *J. Chem. Phys.* **68** 160

[70] Bakr W S, Peng A, Tai M E, Ma R, Simon J, Gillen J I, Foelling S, Pollet L and Greiner M 2010 *Science* **329** 547

[71] Sherson J F, Weitenberg C, Endres M, Cheneau M, Bloch I and Kuhr S 2010 *Nature* **467** 68

[72] Preiss P M, Ma R, Tai M E, Simon J and Greiner M 2015 *Phys. Rev.* A **91** 041602

[73] Boll M, Hilker T A, Salomon G, Omran A, Nespolo J, Pollet L, Bloch I and Gross C 2016 *Science* **353** 1257

[74] Murmann S, Deuretzbacher F, Zürn G, Bjerlin J, Reimann S M, Santos L, Lompe T and Jochim S 2015 *Phys. Rev. Lett.* **115** 215301

[75] Serwane F, Zürn G, Lompe T, Ottenstein T, Wenz A and Jochim S 2011 *Science* **332** 336

[76] Islam R, Ma R, Preiss P M, Tai M E, Lukin A, Rispoli M and Greiner M 2015 *Nature* **528** 77

[77] Schachenmayer J, Weld D M, Miyake H, Siviloglou G A, Ketterle W and Daley A J 2015 *Phys. Rev.* A **92** 041602